INORGANIC CHEMISTRY FRONTIERS

CHINESE CHEMICAL SOCIETY

ROYAL SOCIETY OF CHEMISTRY

RESEARCH ARTICLE

View Article Online
View Journal

Check for updates

Cite this: DOI: 10.1039/d5qi00907c

Pushing boundaries in single molecule magnets: an *ab initio* perspective on harnessing higher oxidation states for unprecedented lanthanide SMM performance†

Tanu Sharma, Rajanikanta Rana, Abinash Swain and Gopalan Rajaraman *

The recent breakthrough of attaining a blocking temperature near liquid N_2 temperature rekindled the interest in lanthanide-based single molecule magnets (SMMs) for end-user applications. Within this realm, several challenges are present, with a key objective being the further enhancement of the blocking temperature. As the current set of molecules based on Dy^{III} have already reached their maximum potential barrier height for magnetisation reversal (U_{eff}), chemical insight-based developments are hampered. To address these challenges, using density functional theory (DFT) and *ab initio* complete active space self-consistent field (CASSCF) methods, we have explored the possibility of obtaining lanthanide SMMs in high-valent oxidation states such as +4 and +5. We begin with various small models of $[LnO_2]^+$, $[LnO_2]$, and $[LnO_2]^-$ (Ln varying from Ce to Lu) systems to correlate the nature of the lanthanides to the SMM characteristics. We have also extended our study to include eight complexes reported earlier possessing +4 and +5 oxidation states to offer clues to improve the SMM characteristics. Our calculations reveal several advantages in fine-tuning the oxidation states in lanthanide SMMs, including the following: (i) increased lanthanide–ligand covalency compared to the Ln^{III} counterpart, (ii) a magnetisation reversal barrier height as high as 8424 cm^{-1}, an unprecedented value compared to any models reported, (iii) among various ways to stabilise such high-oxidation states, encapsulation yielding several targets, with HoO_2@SWCNT(4,4) predicted to yield an impressive energy barrier of ~5400 cm^{-1} and (iv) stronger lanthanide–ligand bonds that were also found to quench spin–phonon relaxation, as they offset the vibrations that cause this relaxation. These potentially yield higher blocking temperatures, offering a novel strategy for developing a new class of lanthanide SMMs.

Received 7th April 2025,
Accepted 23rd April 2025

DOI: 10.1039/d5qi00907c

rsc.li/frontiers-inorganic

Introduction

More than three decades of research into single molecular magnets (SMMs) have brought many breakthrough discoveries. The field has come a long way, from discovering $[TbPc_2]$[1] as the first lanthanide-based single-ion magnet, to achieving blocking temperatures (T_B) in the range of 60–80 K for the dysprosocenium class of molecules,[2–4] and to obtaining a dinuclear $[(CpiPr_5)_2Ln_2I_3]$ molecule featuring a rare lanthanide–lanthanide one-electron bond with an attractive T_B value.[5] The magnetic anisotropy, key to the performance of lanthanide SMMs, is correlated to the crystal field splitting of the ground state m_J levels. Tremendous efforts have been undertaken to modulate the crystal field splitting *via* ligand design, including enhancing the axiality of Dy^{III} complexes using strongly electronegative donor atoms at the axial position such as O^-, $(O^tBut)^-$, $(OPPh)^-$, X^-, *etc*. Additionally, efforts to weaken the equatorial ligand field have proven equally rewarding, as has employing weaker ligands as donors in equatorial positions.[6–10] Alternatively, an external electric field has also been suggested as a tool to modulate magnetic anisotropy.[11] All these efforts have been centred on modulating the ligand field, and one crucial aspect that has gained less attention from the scientific community is the role of the oxidation state of the Ln ions in modulating the anisotropy. This is essential because the majority of the reported Ln complexes exhibit a +3 oxidation state, with some exhibiting species in the +2 oxidation state.[12–15] Also, experimental and theoretical studies

---

Department of Chemistry, IIT Bombay, Powai, Mumbai – 400076, India.
E-mail: rajaraman@chem.iitb.ac.in

† Electronic supplementary information (ESI) available: Structure parameters of the optimised geometries of LnO_2 models, optimised geometries of all the structures not given in the main manuscript, structure of bonding orbitals, parameters computed from AIM analysis, energy of the states (cm^{-1}) along with g_{xx}, g_{yy} and g_{zz} for all the Kramers ions, relaxation mechanisms of the complexes not given in the main manuscript, and spin–phonon coupling of complexes **4** and **5**. See DOI: **https://doi.org/10.1039/d5qi00907c**

show a far greater magnetic moment in divalent complexes than in their trivalent counterparts.[16] Although the magnetic properties of divalent complexes are well known, tetravalent lanthanide complexes are rare.[12,15] However, achieving tetravalency in Ln is challenging as this often requires electron removal from the deeply buried 4f-shells, adding a steep energy penalty. Furthermore, the reduction potentials of Ln^{IV} cations are favourable, making the Ln^{IV} complexes less stable. The Ce ion is known to exhibit a +4 oxidation state, and there are numerous examples documenting this effect.[17,18] Conversely, in bulk systems such as lanthanide oxides or fluorides, Ln^{IV} ions have been unambiguously identified for Tb, Pr, Nd and Dy ions by La Pierre and co-workers.[19] Recently, Mazzanti and co-workers[20] reported a Tb^{IV} complex $[Tb(OSi(O^tBu)_3)_4]$ obtained using a strong oxidising agent such as $[N(C_6H_4Br)_3][SbCl_6]$ (tris(4-bromophenyl)ammonium hexachloroantimonate salt) from the corresponding Tb^{III} precursor. This complex was further characterised using X-ray and magnetic measurements. Also, Pr^{IV} complexes $[Pr^{IV}(OSiPh_3)_4(MeCN)_2]$ have been isolated and found to exhibit exciting luminescence properties.[21] In particular, it is interesting to note that the Pr^{IV} complex is more stable than the Pr^{III} precursor. This opens the door for tetravalent lanthanide complexes. Beyond Ln^{IV} cations, there are also reports of Ln^{V} complexes, though these are currently very limited.[22–24] Moving from Ln^{III} cations to Ln^{IV} cations offers several advantages: (i) a potential enhancement in the crystal field strength and U_{eff} values, though the work of Chibotaru and co-workers[16] found only marginal improvements in crystal field strength and U_{eff} values upon moving to a higher oxidation state (from +2 to +3), and (ii) the Ln–L ligand bond is expected to be strengthened, leading to an increase in the corresponding phonon frequency strength. This effect has the potential to disrupt the spin–phonon relaxation process,[25,26] thereby increasing the blocking temperature. Consequently, these properties make Ln^{IV} cations a promising candidate for the development of advanced materials with enhanced responsiveness to external influences.

Undoubtedly, the theoretical studies employing CASSCF/RASSI-SO/SINGLE_ANISO methods have significantly shaped the design and advancement of molecular magnets. In particular, fundamental work related to the development of the relaxation mechanism for simple models such as Dy^{III}–O, Dy^{III}–$(OH)_2$ and Dy^{III}–F[27,28] helped experimentalists design suitable ligand architecture, leading to superior Dy SIMs. In this connection, here, employing density functional methods and *ab initio* CASSCF calculations, we have studied various models such as $[LnO_2]^+$, $[LnO_2]$ and $[LnO_2]^-$ (Ln varies from Ce to Lu) with different Ln ions. In addition, our investigation extends to nearly all experimentally synthesised Ln^{IV} and Ln^{V} complexes, aiming to present a more authentic portrayal. Our study also includes lanthanocene complexes, considering their extensively researched spin–phonon coupling properties, to understand the role of the enhanced oxidation state on spin–phonon relaxation – providing design clues for new-generation SIMs in this uncharted territory. We initiated our study by utilising small hypothetical models to assess how the oxidation state impacts both structural and magnetic properties. Using these assessments, we formulated predictions regarding potential structures and subsequently advanced to analyse the magnetic properties exhibited by real-world examples.

Results and discussion

Toy models with in-depth electronic and magnetic properties

We have optimised all $[LnO_2]$ and $[LnO_2]^-$ models using both DFT and CASSCF methods. While the DFT-optimized structures exhibit similar trends (results provided in the ESI†), the CASSCF-optimized geometries (Tables S2 and S3†), better suited for capturing metal anisotropy and handling orbitally degenerate ground states, have been chosen for further analysis of the small model systems. We have observed no noticeable trends in structural parameters with respect to the individual lanthanide ions across the series (Tables S2 and S3†). Initially, we optimised four small models, denoted as $[EuO_2]^{2-}$, $[GdO_2]^-$, $[TbO_2]$, and $[DyO_2]^+$, where the lanthanide elements are in oxidation states +2, +3, +4 and +5, respectively, and all the ions are in an f^7 configuration, to exclusively examine the variation in the crystal field due to the different oxidation states, without considering the spin–orbit effect and shape. The calculated Ln–O distances were 2.266 Å and 1.862 Å for $[EuO_2]^{2-}$, 1.996 Å and 2.117 Å for $[GdO_2]^-$, 1.839 Å and 1.839 Å for $[TbO_2]$ and 1.771 Å and 1.771 Å for $[DyO_2]^+$, accompanied by an O–Ln–O bond angle of 180° for all (Fig. 1(a)–(d)). While $[EuO_2]^{2-}$ and $[GdO_2]^-$ exhibit O═Ln–O like character, both bonds in $[TbO_2]$ and $[DyO_2]^+$ are equal in length. The calculated crystal field splitting (CFS) computed from *ab initio* ligand field theory (AILFT) was 5012 cm^{-1}, 5924 cm^{-1}, 26 225 cm^{-1} and 113 480 cm^{-1} for the +2, +3, +4 and +5 oxidation states, respectively, with crystal field parameters provided in Table S1.† Notably, the crystal field splitting increased approximately 1.25, 5 and 4 times when moving from the +2 to +3, +3 to +4 and +4 to +5 oxidation states, respectively (Fig. 1(e)). This highlights the significance of increasing the oxidation state in modulating the anisotropy. In all these models, since there are ligands only along the z-axis, the orbitals having z-components were found to be energetically raised, with $4f_{z^3}$ exhibiting the highest energy (Fig. 1(e)).

Atoms in molecule (AIM) analysis within the DFT framework was conducted to compare the nature of the Ln–O bonds. Although Ln^{III} complexes are primarily ionic with a small covalent bonding contribution,[29–31] we have observed an increased covalency in Ln^{IV} complexes. The analysis revealed that Ln^{IV}–O bonds exhibit significantly higher covalency compared to the Ln^{III}–O counterpart, with the most pronounced variations observed for lighter lanthanides and minimal variations for heavier lanthanides (see Computational details, Fig. 1(f), Fig. S1, S2, and Tables S4, S5†). The $|V(r)|/G(r)$ ratio indicates bond character, with values <1 signifying ionic bonds, >2 indicating covalent bonds, and intermediate values suggesting mixed character; this trend is reflected in the

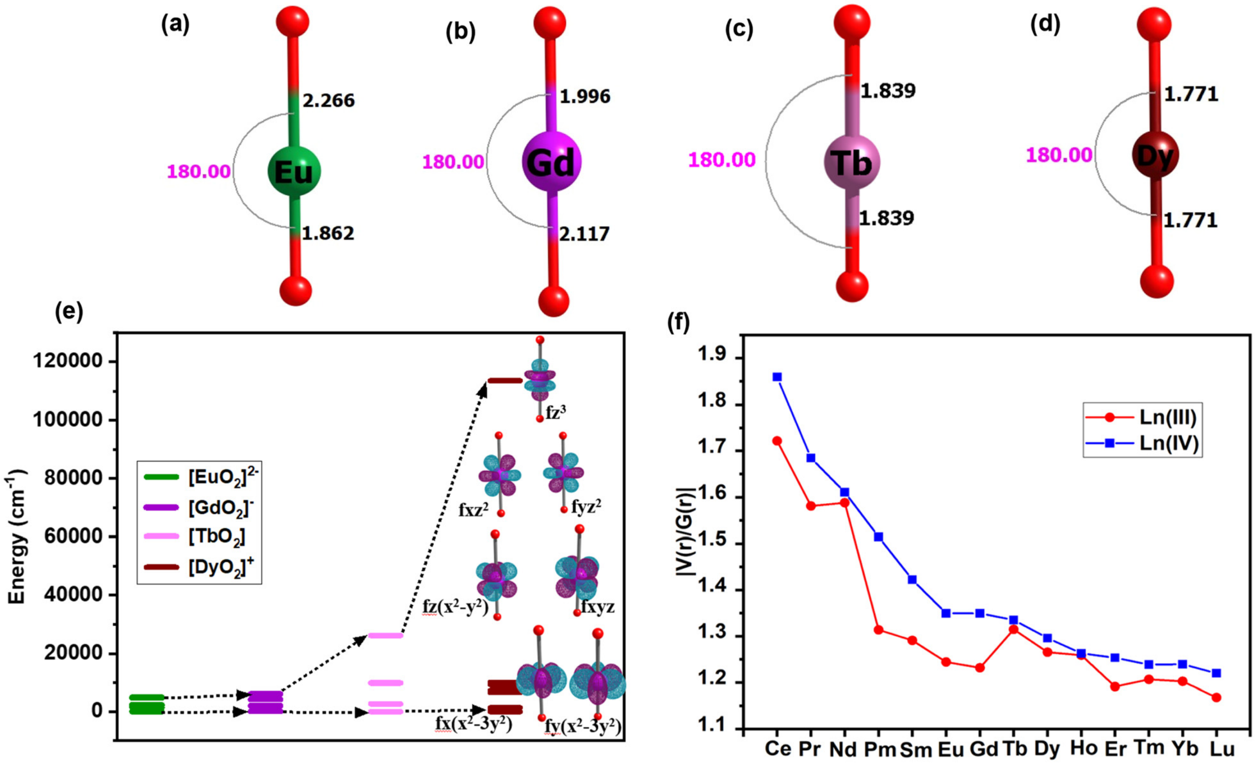

Fig. 1 CASSCF optimised structures of (a) $[EuO_2]^{2-}$, (b) $[GdO_2]^{-}$, (c) $[TbO_2]$, and (d) $[DyO_2]^{+}$; (e) relative energies of 4f orbitals in $[EuO_2]^{2-}$, $[GdO_2]^{-}$, $[TbO_2]$ and $[DyO_2]^{+}$ complexes obtained from *ab initio* ligand field theory (AILFT) analysis; and (f) $|V(r)/G(r)|$ ratios of different lanthanide ions from Ce to Lu in different oxidation states. Colour code: Ln^{II}: green, Ln^{III}: magenta, Ln^{IV}: pink, Ln^{V}: maroon and O: red. The black text around the bonds represents the bond distance in Å, and the fuchsia text represents the bond angle in °.

higher $|V(r)|/G(r)$ ratios observed for Ln^{IV} complexes compared to Ln^{III} complexes. The increase in covalency in $Ln^{IV}O_2$ in comparison with $Ln^{III}O_2$ can also be observed from the higher bond order in the former than in the latter, as shown in Table S6† (except for the structures where the model is bent in its optimised structure). The decrease in covalency from Ce to Yb can be attributed to two factors: (i) a reduction in the number of f-electrons available for bonding and (ii) a decrease in the ion size due to lanthanide contraction. The larger size of lighter lanthanides leads to more diffuse outer electrons, making them more susceptible to covalent bonding. On the other hand, the observed increase in covalency across different oxidation states can be attributed to the difference in the CFS. It was found that the 4f orbitals in $[TbO_2]$ and $[DyO_2]^{+}$ models are energetically higher than those in $[EuO_2]^{2-}$ and $[GdO_2]^{-}$ models (see Fig. 1(e)). This suggests that the larger charge on the metal-ion and, hence, the large negative charge on the neighbouring ligands destabilise the 4f orbital energies, bringing them closer to the ligand molecular orbitals in the +4 oxidation state, enhancing covalency and the crystal field (*vide infra*). The computed parameters indicate a substantial increase in CFS for +4 models, with values comparable to those of transition metal ions[32,33] implying that Ln^{4+} models are likely to behave more like transition metal ions in terms of CFS. Additionally, $[LnO_2]^{2-}$, $[LnO_2]^{-}$, $[LnO_2]$ and $[LnO_2]^{+}$ models obtained from DFT calculations also yield similar structural parameters, enhancement in CF strength and covalency, affirming the trend obtained from CASSCF-optimised geometries (Fig. S3 and Tables S7–S9†).

To provide further insights[34] into the difference in the magnetic properties of $[LnO_2]$, $[LnO_2]^{-}$ and $[LnO_2]^{+}$ complexes, CASSCF/RASSI-SO/SINGLE_ANISO calculations were performed on the model structures. *Ab initio* calculations reveal the highest energy barrier for the spin-reversal (U_{cal}) value of 8424 cm^{-1} for $[ErO_2]^{+}$, 5680 cm^{-1} ($\mu_B = 2.8$) for $[HoO_2]$, and 1765 cm^{-1} for trivalent $[DyO_2]^{-}$ (Fig. 2(a)–(c) and Tables S10–S14†). In all these systems, relaxation occurs from the fourth excited state; however, variations in crystal field splitting significantly impact the U_{cal} values. These values are notably elevated, exceeding the maximum limit of 2085 cm^{-1} for +3 systems.[27] The primary factor behind these exceptionally high U_{cal} values is the presence of robust Ln–O bonds.

Other $[LnO_2]^{-}$ complexes, namely $[CeO_2]^{-}$, $[PrO_2]^{-}$, $[NdO_2]^{-}$, $[SmO_2]^{-}$, $[TbO_2]^{-}$ and $[HoO_2]^{-}$, have U_{cal} values of 1274 cm^{-1}, 2093 cm^{-1}, 1997 cm^{-1}, 295 cm^{-1}, 1886 cm^{-1} and 371 cm^{-1}, respectively (Tables S10–S14 and Fig. S4†). However, for the +4 series, $[PrO_2]$, $[NdO_2]$, $[PmO_2]$, $[DyO_2]$, and $[ErO_2]$ were found to have energy barriers of 1386 cm^{-1}, 2621 cm^{-1}, 2454 cm^{-1}, 1144 cm^{-1} and 4072 cm^{-1}, respectively (Tables S10–S14 and Fig. S5†). Among the pentavalent ions, $[NdO_2]^{+}$, $[PmO_2]^{+}$ and

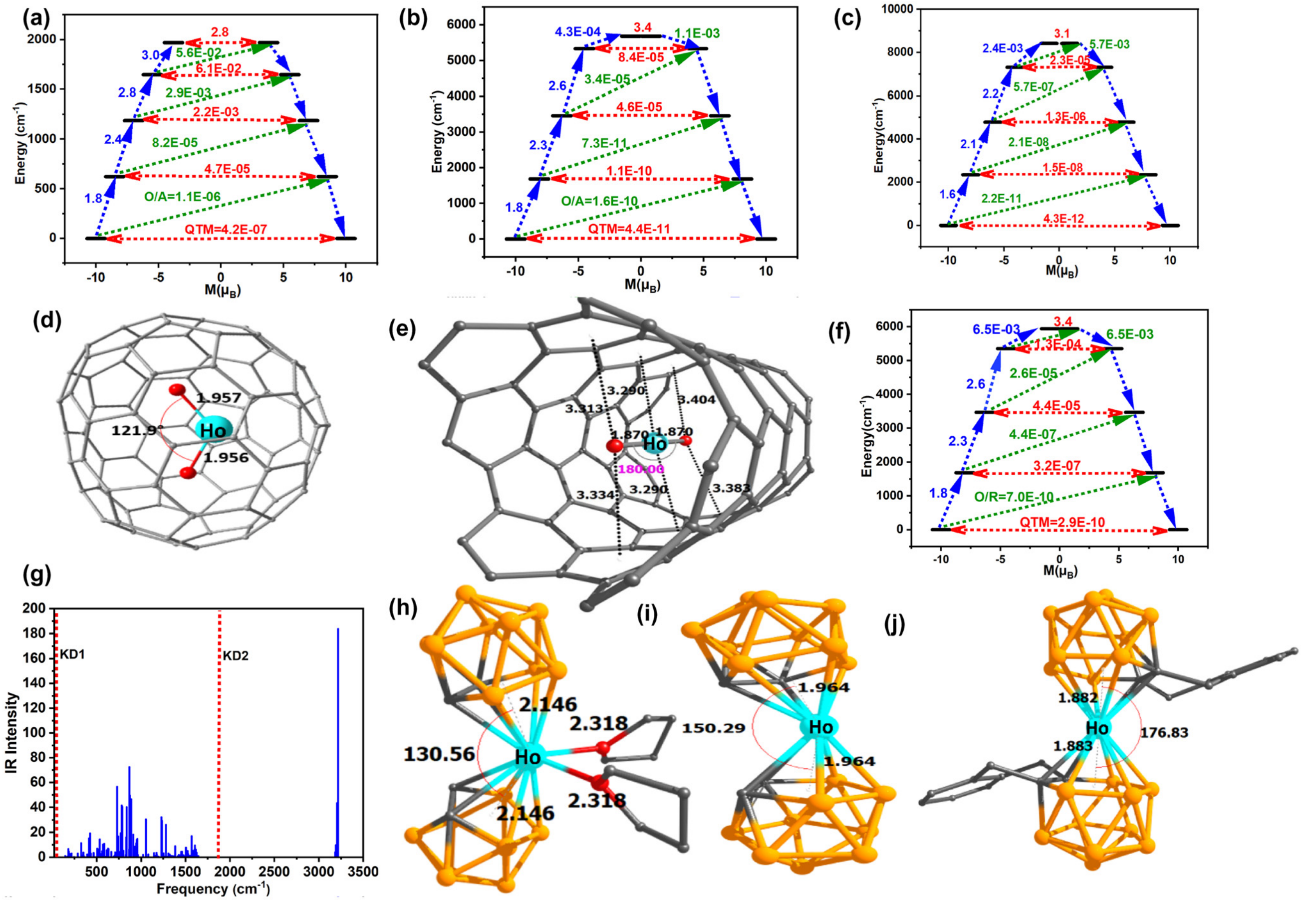

Fig. 2 *Ab initio* computed magnetic relaxation mechanism of hypothetical (a) $[DyO_2]^-$, (b) $[HoO_2]$, and (c) $[ErO_2]^+$; DFT optimised structure of (d) **m1** and (e) **m2**; (f) mechanism for magnetic relaxation in **m2**; (g) plot between IR intensity and frequency in **m4**; DFT optimised structure of (h) **m3**, (i) **m4**, and (j) **m5**. Colour code: Ho: cyan, C: grey, O: red, and B: orange. Hydrogens are omitted for clarity. The black text around the bonds represents the bond distance in Å, and the black text around the angles represents the bond angle in °. In the magnetization relaxation diagram, the thick black line indicates the KDs as a function of the computed magnetic moment. The green/blue arrows show the possible pathway through Orbach/Raman relaxation. The dotted red lines represent the presence of QTM/TA-QTM between the connecting pairs. The numbers provided at each arrow are the mean absolute values for the corresponding matrix element of the transition magnetic moment.

$[HoO_2]^+$ were found to have energy barriers of 2946 cm^{-1}, 3015 cm^{-1} and 1324 cm^{-1}, respectively (Tables S10–S14 and Fig. S6†). Apart from these models, all the remaining models do not show any SMM behaviour due to larger quantum tunnelling of magnetisation (QTM) in Kramers ions and large tunnel splitting in non-Kramers ions.

Encapsulated and other literature-inspired models

Despite the significant Ln–ligand covalency observed in these models, the +4 oxidation state of Ln ions is unstable without a suitable ligand environment.[20,21] For instance, most of the reported Ln^{IV} complexes are not air-stable and either decompose rapidly or remain stable in solution. There are various methods available for stabilising such unstable structures, including cage encapsulation, as demonstrated in stabilising higher oxidation states of transition metals/actinides.[35,36] Molecules such as Mn_{12} and $TbPc_2$ have been encapsulated in single-walled carbon nanotubes (SWCNTs),[37,38] which have been found to offer better performance. Endohedral metallofullerenes (EMF) provide promising opportunities for stabilising small structural motifs such as $\{Dy_2ScN\}$ and $\{Dy_2O\}$ inside the cage.[39–42] Several such geometries were predicted by our group[43–45] and later verified by experimental groups.[46,47] Furthermore, Yamashita and co-workers recently reported the synthesis and magnetic characterisation of $[Dy(cp)_3]$@SWCNT,[48] suggesting a possible way forward to stabilise unstable molecules and also found significant enhancement in the CFS upon encapsulation, as suggested earlier by our group.[44]

Motivated by these studies, we considered the encapsulation of $[HoO_2]$ inside C_{82}, yielding $HoO_2@C_{82}$ (**m1**), and inside SWCNT, leading to HoO_2@SWCNT(4,4) (**m2**) complexes. We observed that the $[LnO_2]$ geometry undergoes deformation upon encapsulation (binding energy −329 kJ mol^{-1}) in **m1**. The Ln–O bond distance is approximately 1.957 Å, while the O–Ln–O bond angle is 121.9°. However, in **m2** (binding energy −375 kJ mol^{-1}), the geometry remains linear with an Ln–O bond distance of 1.870 Å. Very strong (several O⋯π distances of <3.4 Å) anion⋯π interactions between the molecule and the SWCNT were noted, which yield large binding energy and also suggested a possible way to entrap and stabilise such species that are reported earlier in gas phase experiments.[24]

To investigate the influence of encapsulation on the magnetic properties, we have performed *ab initio* calculations on **m1** and **m2** (Fig. 2(d) and (e)). These calculations yielded an energy barrier of approximately 2564 $\mathrm{cm^{-1}}$ for **m1**, which is lower than that of the free [$\mathrm{LnO_2}$] model (Fig. S7(a)† and 2(b)). The comparatively smaller energy barrier than that of free [$\mathrm{LnO_2}$] can be attributed to two main factors. Firstly, bending the O–Ln–O angle within the encapsulating cage by 58° plays a significant role. Secondly, weak Ln⋯C interactions were identified, contributing to a minor transverse anisotropy effect, subsequently enhancing the QTM probability in all the Kramers doublets (KDs). Meanwhile, for **m2**, the U_{cal} value came out to be 5394 $\mathrm{cm^{-1}}$ (Fig. 2(f)), similar to toy models. Relaxation here also occurs from the fourth excited state. Although the structure remains linear, the bond distance is slightly smaller than that of the free [$\mathrm{LnO_2}$] (1.870 Å *vs.* 1.819 Å). As a result, the U_{cal} value also turns out to be comparable but slightly smaller than that of the free [$\mathrm{LnO_2}$]. It is noteworthy that encapsulated models can retain U_{cal} values as large as 5000 $\mathrm{cm^{-1}}$. Furthermore, careful analysis of the molecular vibrations reveals that in the range of 1650–3150 $\mathrm{cm^{-1}}$, no vibrations exist. The KD1–KD2 gap of 1780 $\mathrm{cm^{-1}}$ computed for **m2** falls within this window, meaning that no vibrations or phonons can relax the magnetisation. This offers a rare chance of completely quenching spin–phonon coupling *via* the Orbach process in this molecule (Fig. 2g).

Furthermore, inspired by the work of Zheng and colleagues,[49,50] we expanded our calculations to include dicarbolide-type ligands possessing di- and tetranionic ligands. We examined two types within this class, namely *nido*-$\mathrm{C_2B_9H_{11}}^{2-}$, which is isoelectronic with cyclopentadienyl, and *arachno*-$\mathrm{C_2B_{10}H_{10}}$, which is tetraanionic, and hence expected to stabilise even larger oxidation state Ln ions. We performed DFT calculations on three complexes: [$\mathrm{(C_2B_9H_{11})_2Ho^{IV}(THF)_2}$] (**m3**) and [$\mathrm{(C_2B_9H_{11})_2Ho^{IV}}$] (**m4**) containing dianionic ligands and [$\{\mu\text{-}1,2\text{-}[o\text{-}\mathrm{C_6H_4(CH_2)_2}]\text{-}1,2\text{-}\mathrm{C_2B_{10}H_{10}}\}_2\mathrm{Ho^{IV}}]^{4-}$ (**m5**) possessing a tetranionic ligand (Fig. 2(h)–(j)). In **m3**, the centroid1–Ho–centroid2 angle was found to be 130°, which is higher than the one reported for $\mathrm{Dy^{III}}$ (128°) X-ray geometry. At the same time, the centroid1–Ho and centroid2–Ho bond distances are both found to be 2.145, which is shorter than the experimentally reported values for $\mathrm{Dy^{III}}$. Both these factors support the higher energy barrier of 875 $\mathrm{cm^{-1}}$ in **m3** (Fig. S7(b)†) as compared to the experimentally reported value of 299 $\mathrm{cm^{-1}}$ for the $\mathrm{Dy^{III}}$ complex. In **m4**, the removal of THF solvent ligands results in a higher bond angle of 150° and shorter bond distances of 1.964 Å. This leads to an energy barrier of 1881 $\mathrm{cm^{-1}}$, as expected (Fig. S7(c)†). With the shorter Ho–ligand distance, it is anticipated that the additional THF present in the $\mathrm{Dy^{III}}$ geometry may no longer coordinate and is expected to yield performant SMMs. For **m5**, the centroid is hexagonal in nature and the centroid1–Ho–centroid2 bond angle is found to be 176°, which is higher than the reported value of 153° for the corresponding $\mathrm{Dy^{III}}$ X-ray geometry.[49,50]

Similarly, it also exhibits shorter bond distances of 1.882 Å and 1.883 Å for centroid1–Ho and centroid2–Ho, respectively. The energy barrier for spin-reversal, in this case, is 280 $\mathrm{cm^{-1}}$ (Fig. S7(d)†). This lower energy barrier may be attributed to the stronger equatorial field from the hexagonal ring in **m5** compared to the pentagonal rings in **m3** and **m4**. Nevertheless, the barriers in predicted $\mathrm{Ho^{IV}}$ geometries surpass those reported for $\mathrm{Dy^{III}}$, thus establishing promising synthetic targets.

Deciphering magnetization relaxation mechanisms using X-ray structures of complexes 1–3 featuring $\mathrm{Ln^{IV}}$ cations

Having thoroughly investigated $\mathrm{Ln^{IV}}$ models and proposed their stabilisation through encapsulation, our attention now turns to examining reported $\mathrm{Ln^{IV}}$ molecules with X-ray geometries. In particular, we have performed *ab initio* calculations on the X-ray structures of the complexes [$\mathrm{Tb^{IV}(OSi(O^tBu)_3)_4}$] (**1**),[20] [$\mathrm{Pr^{IV}(OSiPh_3)_4(MeCN)_2}$] (**2**)[51] and [$\mathrm{Ce^{IV}(O)(NR_2)_3}]^{+}$ (**3**).[17] Complex **1** displays diamagnetic behaviour, whereas **2** is isotropic in nature ($4f^7$ configuration), and **3** exhibits a notably high QTM. Furthermore, in order to investigate the magnetic properties of $\mathrm{Ho^{IV}}$, we replaced $\mathrm{Tb^{IV}}$, $\mathrm{Pr^{IV}}$, and $\mathrm{Ce^{IV}}$ ions with $\mathrm{Ho^{IV}}$ (designated as **1**-Ho, **2**-Ho and **3**-Ho; Fig. 3(a)–(c)), as $\mathrm{Ho^{IV}}$ has been shown in the earlier section to exhibit superior SMM characteristics among all $\mathrm{Ln^{IV}}$ ions.

In complex **1**-Ho, we observed a large QTM, and hence, the absence of SMM characteristics is expected. On the other hand, the magnetisation relaxation mechanism established for complex **2**-Ho reveals that relaxation occurs *via* the third KD, imparting an energy barrier of 725 $\mathrm{cm^{-1}}$ (Fig. 3(d)). Furthermore, in complex **3**-Ho, the stronger ligand field provided by the Ln═O bond results in a higher energy barrier of 1299 $\mathrm{cm^{-1}}$ compared to **2**-Ho (Fig. 3(e)). Although the geometry of these complexes is unfavourable for exhibiting a large energy barrier (pseudo-octahedral/tetrahedral geometries), variations in the Ln–O distances and the nature of the $\mathrm{Ln^{IV}}$–O bonding result in a large barrier, supporting the idea of employing this cation even under symmetric conditions to obtain performant SMMs. This further supports the significance of the tetravalent oxidation state in influencing the magnetic properties of these systems.

Comparative analysis of magnetisation and spin–phonon relaxations in +4 and +3 lanthanoarene complexes

Furthermore, we have probed some well-known dysprosocenium complexes, namely [$\mathrm{Dy(Cp^{iPr_5})_2}]^{+}$ (**4**-Dy)[4] and [$\mathrm{(Cp^{iPr_5})Dy(Cp^{*})}]^{+}$ (**5**-Dy)[2] and their *in silico* +4 counterparts [$\mathrm{Ho(Cp^{iPr_5})_2}]^{2+}$ (**4**-Ho) and [$\mathrm{(Cp^{iPr_5})Ho(Cp^{*})}]^{2+}$ (**5**-Ho), where $\mathrm{Cp^{iPr_5}}$ = penta-isopropyl cyclopentadienyl and Cp* = pentamethyl cyclopentadienyl (Fig. 4(a)–(d)). The Dy–C bond distance is 2.375–2.377 Å in **4**-Dy, whereas it falls to 2.232–2.238 Å in **4**-Ho. Consequently, this reduction in bond distance causes the substituents on the *Cp* ring to approach each other, resulting in steric hindrance, which leads to a decrease in the C–Ho–C bond angle. In the **4**-Ho complex, there is a notable decrease

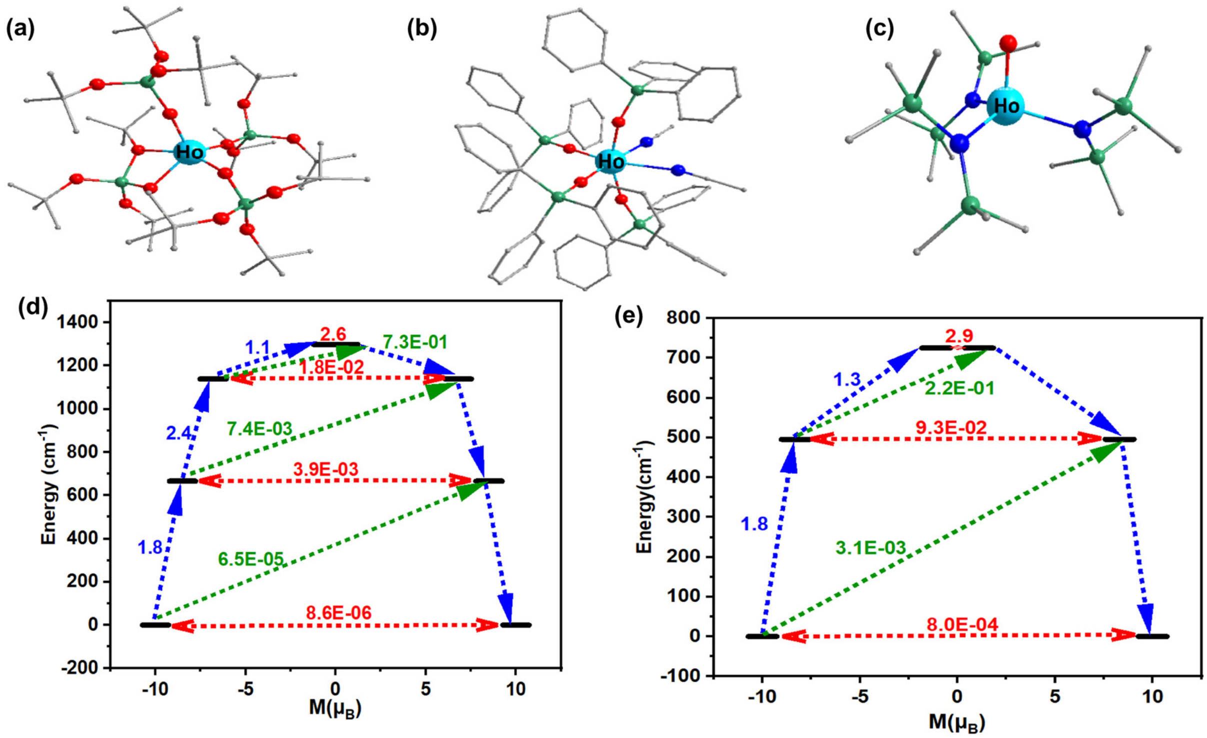

Fig. 3 X-ray structure of (a) **1**-Ho, (b) **2**-Ho, and (c) **3**-Ho; and their mechanism of magnetization relaxation for (d) **2**-Ho and (e) **3**-Ho. Colour code: $\mathrm{Ln^{IV}}$: cyan, O: red, C: grey, N: blue, and Si: green. Hydrogens have been omitted for clarity. In the magnetization relaxation diagrams, the thick black line indicates the KDs as a function of the computed magnetic moment. The green/blue arrows show the possible pathway through Orbach/Raman relaxation. The dotted red lines represent the presence of QTM/TA-QTM between the connecting pairs. The numbers provided at each arrow are the mean absolute values for the corresponding matrix element of the transition magnetic moment.

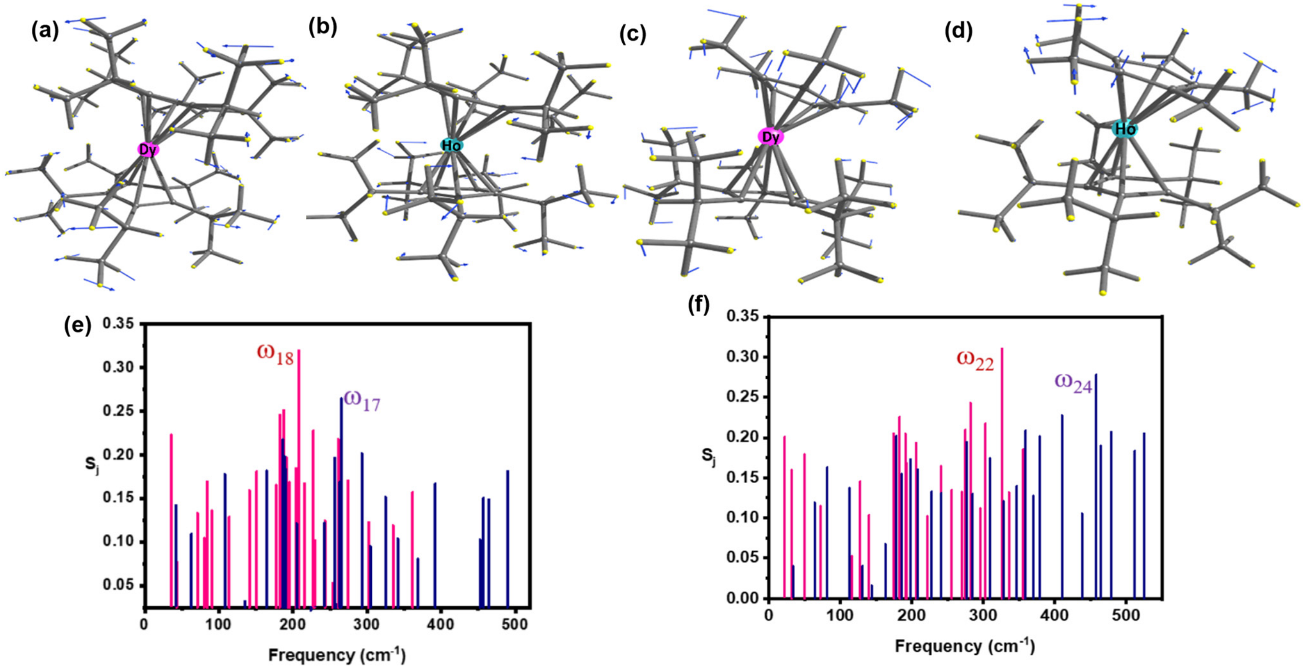

Fig. 4 (a) The molecular vibration of **4**-Dy corresponds to ω_{18} (cm^{-1}). (b) The molecular vibration of **4**-Ho corresponds to ω_{18} (cm^{-1}). (c) The molecular vibration of **5**-Dy corresponds to ω_{18} (cm^{-1}). (d) The molecular vibration of **5**-Ho corresponds to ω_{24} (cm^{-1}). (e) The coupling strength for the high-intensity vibrational modes of **4**-Dy (pink) and **4**-Ho (blue). (f) The coupling strength for the high-intensity vibrational modes of **5**-Dy (pink) and **5**-Ho (blue). Colour code: $\mathrm{Ho^{IV}}$: cyan, $\mathrm{Dy^{III}}$: pink, and C: grey. Hydrogens are omitted for the clarity.

of approximately 0.096 Å in the bond distance compared to **4**-Dy. It is worth mentioning that the U_{cal} value of **4**-Dy (1383 cm^{-1}) is comparable to the experimentally reported effective anisotropy energy (U_{eff}) determined from the X-ray structure (1334 cm^{-1}), which is significantly smaller than the one reported for **4**-Ho (1785 cm^{-1}) (Fig. S8(a) and S8(b)†). Similarly, **5**-Ho has a U_{cal} value of 1694 cm^{-1}, which is higher than that of **5**-Dy (1223 cm^{-1}) by 471 cm^{-1} (Fig. S8(c) and S8(d)†). The smaller and stronger Ho–C bond distances in Ho^{IV} metallocene than in Dy^{III} metallocene will likely result in a greater energy penalty for bending of the *Cp* ring that is associated with the corresponding vibrations that are responsible for relaxation in dysprosocenium complexes.[2] Therefore, the higher energy penalty for bending is expected to shift the corresponding vibrations to larger values, making them off-resonance with the spin–phonon relaxation and hence can aid in enhancing the T_{B} values. Also, as the U_{eff} values are also suggested to correlate to the T_{B} values, a larger U_{eff} value with a greater oxidation state suggests a larger blocking temperature for this class of molecules.

To understand the role of the oxidation state in spin–phonon coupling in **4**-Dy, we have calculated the spin-vibrational coupling strength (S_j) for selected frequencies with significant oscillatory strengths, as depicted in Fig. 4(e) and Table S15.† This analysis indicates that the ω_{18} vibrational modes with strong coupling are probable contributors to magnetisation relaxation. Additionally, the proximity of the second excited state of the vibrational mode ω_{18} (486 cm^{-1} $((2+\frac{1}{2})\hbar\omega)$) compared to the KD1–KD2 (499 cm^{-1}) energy gap further supports its potential involvement in magnetisation relaxation. Furthermore, we analysed the S_j values for specific vibrational modes of **4**-Ho, as shown in Fig. 4(e) and Table S16.† This analysis reveals that vibrational modes with strong coupling, such as ω_{17}, are likely to influence magnetisation relaxation. Moreover, the close proximity of the second excited state of the vibrational mode ω_{17} (653 cm^{-1}, $(2+\frac{1}{2})\hbar\omega$) is comparable to the KD1–KD2 (650 cm^{-1}) energy gap, further supporting its significant role in magnetisation relaxation. In both **4**-Dy and **4**-Ho, C–H vibrations are identified as the vibrations that lead to relaxation, similar to what is commonly observed in $[(\text{Cp}^{\text{ttt}})_2\text{Dy}]^+$ type molecules (Fig. 4(a) and (b)).[3]

In **5**-Dy, the S_j values for the 24 selected vibrational modes are depicted in Fig. 4(f), with comprehensive data provided in Table S17.† In particular, the vibrational mode ω_{22} exhibits significant coupling strength, suggesting its role in triggering magnetization relaxation. Furthermore, the first excited state of the ω_{22} vibrational mode at 490 cm^{-1} $((1+\frac{1}{2})\hbar\omega)$ closely matches the KD1–KD2 energy gap of 491 cm^{-1}, reinforcing the likelihood of this mode's involvement in magnetisation relaxation. In **5**-Ho, we focused on 30 vibrational modes (Table S18†). The coupling strength of these vibrational modes, as illustrated in Fig. 4(f), indicates that the ω_{26} mode, characterized by high coupling strength, likely contributes to magnetisation relaxation. Furthermore, the proximity of the first excited state of the ω_{26} mode (658 cm^{-1} $((1+\frac{1}{2})\hbar\omega)$) to the KD1–KD2 energy gap of 648 cm^{-1} lends further support to its involvement in magnetisation relaxation. In both **5**-Dy and **5**-Ho, out-of-plane bending of the *Cp** rings was found to initiate the transition from the ground state to the first excited state (Fig. 4(c) and (d)).

These calculations reveal a significant upward shift in vibrational modes when transitioning from Dy^{III} to Ho^{IV}. This shift indicates that the vibrational frequencies of the modes increase with the higher oxidation state of the metal. Additionally, there is a noticeable decrease in the S_j value (Fig. 4(e) and (f)), which represents the vibronic coupling strength. This decrease suggests that the interaction between the spin states and vibrational modes weakens as the metal oxidation state increases, offering a chance to enhance the T_{B} values by quenching the spin–phonon relaxation mechanism *via* the Orbach process. Due to stronger metal–ligand bonds and a more rigid framework, the Raman vibrations are anticipated to shift to higher energies, as evidenced by the calculated vibrational features. This suggests a promising approach for enhancing the T_{B} values in this class of molecules.

Relaxation mechanism in reported Ln models/complexes in the +5 oxidation state

In pursuit of lanthanides with high-valent oxidation states, we encountered some structures exhibiting a +5 oxidation state. To comprehensively investigate the impact of this higher oxidation state, we selected specific complexes and performed *ab initio* calculations on them. Additionally, we extended our research to Ln^{V}–metallocene complexes to facilitate a meaningful comparison with their +3 and +4 counterparts. One of the notable complexes, $[\text{Pr}^{\text{V}}\text{O}_2(\text{NO}_2)_2]^-$ (**6**), reported[23] was characterised using mass spectrometry, although it was air-unstable. Its structural validity was confirmed through extensive computational methods. By substituting Er^{V} in place of Pr^{V}, we performed *ab initio* calculations on $[\text{Er}^{\text{V}}\text{O}_2(\text{NO}_2)_2]^-$ (**6**-Er) (Fig. 5(a)), which exhibited a remarkably high QTM effect and did not exhibit any SMM behaviour (Fig. S9†). Another class of Ln^{V} complexes documented in the literature includes pentavalent nitride oxides with N≡Pr bonds, represented by $[\text{NPr}^{\text{V}}\text{O}]^-$ (**7**) complexes. These are stabilised only by the matrix isolation technique and were detected by IR spectroscopy.[24] Similar to other reported Ln^{V} complexes, this species is also unstable. However, there is substantial evidence in the literature[35,36] showing that stabilising such unstable species or fragments through encapsulation with fullerenes is a viable approach for creating such molecules. Analogous $[\text{NEr}^{\text{V}}\text{O}]^-$ (**7**-Er) (Fig. 5(b)) complexes displayed a significantly high energy barrier of 6243 cm^{-1} for magnetisation (Fig. 5(c)), attributed to very small Pr–O (1.304 Å) and Pr–N (1.104 Å) bond distances and the absence of ligands in the equatorial plane. Our studies were extended to $[(\text{Cp}^{\text{iPr}_5})\text{Er}(\text{Cp}^*)]^{2+}$ (**8**-Er) (Fig. 5(d)), where we observed a C–Er–C bond angle of 145.1, smaller than those of its +3 and +4 counterparts.

Magnetisation relaxation in this complex occurred *via* the first excited state, resulting in a U_{cal} value of 1232 cm^{-1} (Fig. 5(e)), which is lower than those of its +3 and +4 counterparts. The significant reduction in the C–Er–C bond angle is

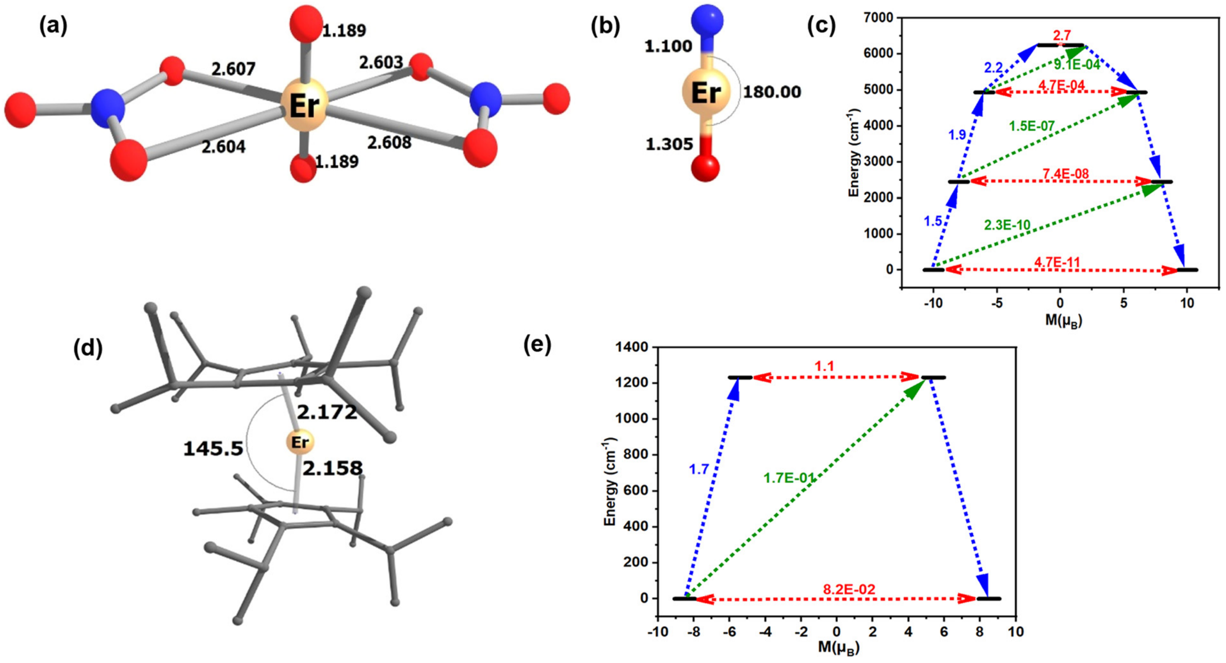

Fig. 5 DFT optimised geometry of (a) **6**-Er, (b) **7**-Er, and (d) **8**-Er; mechanism of magnetization relaxation (c) **7**-Er and (e) **8**-Er. Colour code: Ln^{V}: light golden, O: red, C: grey, N: blue, and Si: green. Hydrogens have been omitted for clarity. The black text around the bonds represents the bond distance in Å, and the black text around the angle represents the bond angle in °. In the magnetization relaxation diagrams, the thick black line indicates the KDs as a function of the computed magnetic moment. The green/blue arrows show the possible pathway through Orbach/Raman relaxation. The dotted red lines represent the presence of QTM/TA-QTM between the connecting pairs. The numbers provided at each arrow are the mean absolute values for the corresponding matrix element of the transition magnetic moment.

the primary factor behind this observation. This alteration now provides an equatorial ligand field, and the smaller Ln–C bond lengths, which were previously advantageous, now become a limiting factor in this context. Additionally, it is important to note within this class of metallocene molecules that higher oxidation states can also impose limitations, as observed in the +5 model. Here, the higher oxidation state induces larger Cp–Ln–Cp bending, which typically results in lower vibrational modes. This bending not only reduces axiality but also contributes to spin–phonon relaxation, which is expected to decrease the overall T_B values. We have also calculated the τ_{QTM} values based on the established protocols,[52–59] which also reflect the generated trend discussed here (see Table S23 in the ESI†).

Conclusions

In this work, we have explored a hitherto unknown approach to enhance the performance of SMMs using tetra and pentavalent lanthanide-based complexes and investigated the impact of enhanced oxidation states on their magnetic properties. To begin with, simple model systems were studied, which showed promising results. We have extended the studies to available complexes containing Ln^{IV} and Ln^{V} oxidation states and predicted a series of models/complexes that yield U_{eff} values exceeding 8424 cm^{-1} and are also found to offset the spin–phonon relaxation, potentially leading to higher blocking temperatures. Our calculations on both models and several complexes reveal a significant enhancement in lanthanide–ligand covalency as we move from the Ln^{III} to the Ln^{IV} oxidation state. This increase is found to be substantial for early lanthanides and significant for late lanthanide elements, offering an unwavering way to fine-tune the lanthanide–ligand covalency. As we move from Ln^{III}–O to Ln^{IV}–O and Ln^{IV}–O to Ln^{V}–O, a 300% and 150% increase in U_{eff} values is observed for the $4f^9$ configuration. The growth is substantial for all elements, though the percentage is not uniform. As the predicted models are attractive, we have also extended the study to encapsulate them in fullerenes or SWCNTs. The latter were found to preserve the performance of SMMs, with HoO_2@SWCNT(4,4) predicted to yield an impressive energy barrier of ~5400 cm^{-1}. We have also performed calculations with dicarbolide-type ligands with dianionic and tetraanionic charges, which are expected to stabilise a higher oxidation state. Our calculations reveal significant improvements over their +3 counterparts within this class of molecules. Particularly noteworthy are models featuring shorter metal–ligand distances, which demonstrate attractive energy barriers of up to 1881 cm^{-1}, making them promising synthetic targets. We have extended the studies to include models of reported complexes possessing +4 and +5 oxidation states, with $[Ho(O)(NR_2)_3]^+$ and $[NEr^{V}O]^-$ complexes displaying remarkable properties, thereby setting targets based on the available reports.

The higher oxidation state Ln complexes not only increase the crystal field splitting and the corresponding barrier heights but also enhance the strength of the lanthanide–ligand bond. This modification markedly reduces the spin–phonon coupling values and vibrational levels in certain scenarios, potentially resulting in larger T_B values. To assess and analyse this aspect, we have modelled lanthanocene molecules in the +4 oxidation state that are found to alter the vibrations and quench the spin–phonon coupling *via* the usual Orbach route – offering a hitherto unknown approach to produce a new class of SMMs.

Computational details

Geometry optimisation employing DFT methods

We have first optimised all small models, namely $[LnO_2]^-$, $[LnO_2]$ and $[LnO_2]^+$ (Table S22†), using DFT methods employing the hybrid B3LYP functional[60–62] using the Gaussian 09 package.[63] Since DFT methods are not well-suited for handling degenerate electronic states, geometry optimizations were performed using the diamagnetic analogues Y, Zr, and Nb to represent the +3, +4, and +5 oxidation states, respectively.

All the models we created that lack experimental precedents, such as encapsulated models or dicarboximide-type complexes, are labelled **m1–m5**. In contrast, complexes with experimental counterparts are numbered **1–8**. When we substitute the metal in these complexes, we name them based on the metal used. For example, these complexes are designated as (**1–8**)-Ho/Er/Dy. Furthermore, we have also performed geometry optimisation using DFT for complexes **4–8** and **m1–m5**. Diamagnetic substitution of Ln^V, Ln^{IV}, and Ln^{III} with Nb^V, Zr^{IV}, and Y^{III} was done in order to reduce the computational cost associated with metallocene and encapsulated models and aid in smooth convergence. We have also optimised small models $[LnO_2]^-$, $[LnO_2]$ and $[LnO_2]^+$ with the same methodology as specified earlier for large molecules. Frequency calculations were performed on all models at the same level of theory and were found to be minima unless otherwise stated. For optimisation, we have used def2-TZVP for Nb, SDD[64] for Y and Zr (triple-zeta with 28 core electrons), TZV for O atoms and 6-31G* for the rest of the atoms for optimisation.[65] The harmonic vibrational modes and vibrational spectra were estimated in metallocene complexes with isotope masses of 162.5 and 164.9 (the masses of the most abundant isotopes of dysprosium and holmium) for Y and Zr to obtain correct reduced masses.[66,67] All geometry optimisations, whether using CASSCF or DFT, were conducted in the gas phase. For single point calculations and atoms-in-molecules (AIM) analysis, we used the CSDZ basis set for Ln ions[66,67] and TZVP for the rest of the atoms. It is noteworthy that the CSDZ basis set has been used for computing exchange coupling and geometry optimisations for Gd^{III} by us and others, demonstrating its effectiveness.[68] Here, the spin-multiplicity of these molecules is as expected; for example, Gd^{III} has a spin-multiplicity of 8, while Gd^{IV} has a spin-multiplicity of 7. We have employed AIM analysis[69] to determine the metal–ligand bonding and identify the bond critical points (BCPs), a method widely recognised for evaluating the nature of bonding in lanthanide complexes.[70,71] According to the AIM theory, the $|V(r)|/G(r)$ ratio indicates the nature of the bond; any value less than 1 indicates an ionic bond and greater than 2 indicates a covalent bond, whereas intermediate values suggest mixed character.[72] Furthermore, we have performed natural bond orbital (NBO) analysis in order to compute Wiberg bond orders using the same level of theory and basis set as those used in QTAIM.

Geometry optimisation using CASSCF methods

All small model optimisations were also performed using the complete active space self-consistent field (CASSCF) approach with the Orca suite.[73] We included all electrons in the 4f orbitals and, to account for Ln–O bonding, added four electrons and six orbitals, including four additional empty orbitals, to the reference space. Various combinations for oxygen orbitals were tested, expanding the reference space stepwise until successful convergence was achieved. Attempts to include orbitals beyond this reference space did not converge, as the bonding orbitals are low-lying in energy and exhibit minimal mixing with the Ln orbitals (Fig. S10†).

First, guess orbitals were optimised using the BP86 level of theory, followed by optimisation at the SA-CASSCF level of theory. A SARC-DKH-TZVP74 basis set was employed for lanthanide ions, whereas a DKH-TZVP75 basis set was used for O atoms. The structural parameters of all the geometries optimised using CASSCF calculations are given in Tables S2 and S3,† and frequency calculations were also performed at the same level for all these geometries. We note that some of the metal–ligand bond distances are asymmetric, which could be attributed to the lack of point group symmetry restrictions, the chosen active space, or the neglect of dynamic correlation.

Estimation of magnetic properties using SINGLE_ANISO

Furthermore, to compute the magnetic anisotropy, *g*-tensors, and the mechanism of relaxation, *ab initio* calculations were performed using MOLCAS 8.2.[74–76] Our study employed atomic natural orbital-type basis sets of the relativistic contracted variety, namely ANO…RCC VTZP (Ln.ANO–RCC…8s7p5d3f2g1 h.) for the lanthanide (Ln) atom and ANO…RCC VDZP[77] (C.ANO–RCC…3s2p1d., O.ANO–RCC…3s2p1d., Si. ANO–RCC…4s3p1d., H.ANO-RCC…2s.) for all other elements. Initially, we generated guess orbitals and selected seven Ln^{III}-based starting orbitals for CASSCF calculations. The spin-free energy was computed using the CASSCF approach,[78] considering multiple roots in the active space, as outlined in Table S19.† The number of these roots depends on the number of electrons present in the seven orbitals. We then utilised the Restricted Active Space State Interaction-Spin Orbital (RASSI-SO) module[79] to determine the spin–orbit coupled states. To extract the corresponding *g*-tensors and energy blockade diagrams, we employed the SINGLE_ANISO code. Furthermore, we performed extended CAS calculations using different CAS for HoO_2(IV) models. These active spaces were

CAS(9,7), CAS(9,11), CAS(9,9), CAS(9,10), and CAS(9,12), respectively. In CAS(9,7), we considered only seven 4f orbitals in the active space. In CAS(9,11), we included 6s + $6p_x$, $6p_y$, and $6p_z$ orbitals along with the seven 4f orbitals. In CAS(9,9), the active space comprised $5d_{z^2}$ and $5d_{x^2-y^2}$ orbitals along with the seven 4f orbitals. Similarly, in CAS(9,10) and CAS(9,12), we included $5d_{z^2}$, $5d_{x^2-y^2}$, $5d_{xy}$ and $5d_z{}^2$, $5d_{x^2-y^2}$, $5d_{xy}$, $5d_{xz}$ and $5d_{yz}$, respectively. We then performed complete active space perturbation theory at second order (CASPT2)[80] calculations on the 21 sextet with an IPEA shift of 0.25 to account for dynamic correlation effects. First, we performed SA-CASSCF calculations to obtain a balanced description of multiple electronic states. The diagonal elements of the effective Hamiltonian, corresponding to these SA-CASSCF energies, were replaced with CASPT2 energies to include dynamic correlation effects using second-order perturbation theory. Estimation of magnetic anisotropy from various methods reveals only a marginal variation, and therefore, the CAS(9,7) set-up was utilised throughout (see Table S20†). In Table S24,† we have summarised all the U_{cal} values and the mode of relaxation in complexes **m1–m5** and **1–8**. For QTM, any value greater than $0.1\mu_{\mathrm{B}}$ is considered sufficient to cause QTM.

Ab initio ligand field theory

Additionally, we employed *ab initio* ligand field theory (AILFT)[81] to determine the crystal field splitting energy (CFSE) using the second-order N-electron valence state perturbation theory (NEVPT2) program employing the ORCA suite 5.0, utilising the same basis set as used in the optimisation. AILFT analysis was applied to $4f^7$-configured complexes in higher oxidation states, where the stronger covalency in $\mathrm{Ln^{IV}}$ leads to significant f-orbital mixing with ligand orbitals, making AILFT essential for projecting maximum orbital contributions and understanding crystal field splitting.

Spin-vibrational relaxation calculations

We performed spin-vibrational relaxation calculations for complexes **4**-Dy, **4**-Ho, **5**-Dy and **5**-Ho. The vibrational frequencies of the complexes were calculated using gas-phase geometry optimisation with DFT, as described in the Computational details section. Subsequent frequency calculations were performed to verify the accuracy of the optimised geometries, confirming that they correspond to true minima on the potential energy surface.[2,3,67,82]

In the absence of any magnetic field, the effective Hamiltonian can be expressed as[83]

$$\hat{H}_{\mathrm{eff}} = \hat{H}_{\mathrm{s}} \otimes \mathrm{II}_{\mathrm{vib}} + \mathrm{II}_{\mathrm{s}} \otimes \hat{H}_{\mathrm{vib}} + \hat{H}_{\mathrm{s\text{-}vib}}$$

where $\hat{H}_{\mathrm{s}}$, $\hat{H}_{\mathrm{vib}}$ and $\hat{H}_{\mathrm{s\text{-}vib}}$ represent the crystal field (spin-system), vibration and spin-vibrational Hamiltonian.

$$\hat{H}_{\mathrm{s}} = \hat{H}_{\mathrm{CF}} = \sum_{k=2,4,6} \sum_{q=-k}^{k} B_k^q \tilde{O}_k^q$$

$$\hat{H}_{\mathrm{vib}} = \sum_j \hbar\omega_j (n_j + 1/2)$$

$$\hat{H}_{\mathrm{s\text{-}vib}} = \sum_j \hat{Q}_j \left(\frac{\partial B_k^q}{\partial Q_j}\right)_0 \tilde{O}_k^q(J)$$

In this context, B_k^q and $\tilde{O}_k^q(J)$ represent the crystal field (CF) parameters and Stevens operators, respectively. The rank k ranges up to $2J$, with the components q varying from $-k$ to $+k$ for each k. The total angular momentum, defined in the M_J basis, ranges from $-M_J$ to $+M_J$ $\left(\text{for } \mathrm{Dy^{3+}} \text{ and } \mathrm{Ho^{4+}},\ J = \frac{15}{2}\right)$ and M_J runs over $\left\{-\frac{15}{2}, -\frac{13}{2}, \ldots, +\frac{15}{2}, +\frac{13}{2}\right\}$. ω_j and n_j correspond to the frequency of the vibrational level of mode j and maximal cartesian displacement vector of a given mode j in its n^th^ harmonic state respectively. $\hat{Q}_j$ and $\left(\frac{\partial B_k^q}{\partial Q_j}\right)_0$ represent the vibrational coordinate and vibronic coupling of mode j, respectively.

The operators $\hat{H}_{\mathrm{s}}$ and $\hat{H}_{\mathrm{vib}}$ in the first equation are defined on the basis of $|M_J, n_j\rangle$ using the Kronecker product. To define $\hat{H}_{\mathrm{s\text{-}vib}}$ on the same basis, we consider a weak coupling regime where the vibrations remain unaffected by the electronic levels. Consequently, $\hat{H}_{\mathrm{s\text{-}vib}}$ can be written as follows:

$$\begin{aligned}
&\left\langle M_j', n_j \pm 1 \middle| \hat{H}_{\mathrm{s\text{-}vib}} \middle| M_j, n_j \right\rangle \\
&\quad = \left\langle M_j', n_j \pm 1 \middle| \sum_{k=2,4,6} \sum_{q=-k}^{k} \hat{Q}_j \left(\frac{\partial B_k^q}{\partial Q_j}\right)_0 \tilde{O}_k^q(J) \middle| M_j, n_j \right\rangle \\
&\quad = \left\langle M_j' \middle| \sum_{k=2,4,6} \sum_{q=-k}^{k} \left(\frac{\partial B_k^q}{\partial Q_j}\right)_0 \tilde{O}_k^q(J) \middle| M_j \right\rangle \times \left\langle n_j \pm 1 \middle| \hat{Q}_j \middle| n_j \right\rangle
\end{aligned}$$

Here, the first term on the right-hand side represents the electronic coupling, and the second term represents the vibrational excitation. To estimate the electronic coupling, we computed the zero-point energy displacements $\left(Q_{j,0} = \sqrt{\frac{\hbar\omega_j}{k_j}}\right.$, where ω_j and k_j denote the frequency and force constant of vibrational mode j). The equilibrium geometry was then distorted within the range of $-Q_{j,0} \rightarrow +Q_{j,0}$ along the displacement vectors ($\vec{v}$) for each mode using:

$$\vec{Q}_{\mathrm{dist},j} = \vec{Q}_{\mathrm{eq}} + \vec{Q}_{j,0}\vec{v}$$

Then, we performed CASSCF/RASSI-SO/SINGLE_ANISO calculations for each distorted geometry ($\vec{Q}_{\mathrm{dist},j}$) and extracted the crystal field parameters (CFPs) in Stevens notation. The extracted CFPs were then fitted using second-order polynomials to obtain the first-order vibronic couplings $\left(\frac{\partial B_k^q}{\partial Q_j}\right)_0$. The overall vibronic coupling strength (S_j) of a given mode is extracted by adding the effect of CFPs as follows:

$$S_j = \sqrt{\frac{1}{3} \sum_k \frac{1}{2k+1} \sum_{q=-k}^{+k} \left| \left(\frac{\partial B_k^q}{\partial Q_j}\right)_0 \right|^2}$$

The energies of the vibrational modes were calculated using the $\left((1 + \frac{1}{2})\hbar\omega\right)$ formula, with the frequencies scaled according to the basis set and functional used.[84] We calculated S_j only for the vibrational modes with large oscillator strength (e^2emu^{-1}), thereby reducing the computational cost of these calculations. Although sometimes referred to as spin–phonon relaxation, these calculations are actually spin-vibrational in nature.

For **5**-Ho, we also performed detailed calculations for all the vibrational modes, and it was found that the vibrational mode with the highest spin–phonon coupling constant ($458.4\ cm^{-1}$) remains the highest in both sets of calculations (Table S21, Fig. S11 and Table S17†), confirming the reliability of our methodology.

Data availability

All data supporting the findings of this study are included in the ESI.† This includes the structure parameters of the optimised geometries of LnO_2 models, optimised geometries of all the structures not given in the main manuscript, structure of bonding orbitals, parameters computed from AIM analysis, energy of the states (cm^{-1}) along with g_{xx}, g_{yy} and g_{zz} for all the Kramers ions, relaxation mechanisms of the complexes not given in the main manuscript, and spin–phonon coupling of complexes **9** and **10**.

Conflicts of interest

There are no conflicts to declare.

Acknowledgements

T. S. is thankful to CSIR India for providing the SRF, R. R. is thankful to PMRF for the fellowship, and A. S. is thankful to IITB for the IPDF. G. R. would like to thank SERB (SB/SJF/2019-20/12; CRG/2022/001697) for funding.

References

1 N. Ishikawa, M. Sugita, T. Ishikawa, S.-y. Koshihara and Y. Kaizu, Lanthanide double-decker complexes functioning as magnets at the single-molecular level, *J. Am. Chem. Soc.*, 2003, **125**, 8694–8695.

2 F.-S. Guo, B. M. Day, Y.-C. Chen, M.-L. Tong, A. Mansikkamäki and R. A. Layfield, Magnetic hysteresis up to 80 kelvin in a dysprosium metallocene single-molecule magnet, *Science*, 2018, **362**, 1400–1403.

3 C. A. Goodwin, F. Ortu, D. Reta, N. F. Chilton and D. P. Mills, Molecular magnetic hysteresis at 60 kelvin in dysprosocenium, *Nature*, 2017, **548**, 439–442.

4 K. R. McClain, C. A. Gould, K. Chakarawet, S. J. Teat, T. J. Groshens, J. R. Long and B. G. Harvey, High-temperature magnetic blocking and magneto-structural correlations in a series of dysprosium(III) metallocenium single-molecule magnets, *Chem. Sci.*, 2018, **9**, 8492–8503.

5 C. A. Gould, K. R. McClain, D. Reta, J. G. Kragskow, D. A. Marchiori, E. Lachman, E.-S. Choi, J. G. Analytis, R. D. Britt and N. F. Chilton, Ultrahard magnetism from mixed-valence dilanthanide complexes with metal-metal bonding, *Science*, 2022, **375**, 198–202.

6 X. L. Ding, Y. Q. Zhai, T. Han, W. P. Chen, Y. S. Ding and Y. Z. Zheng, A Local D4 h Symmetric Dysprosium(III) Single–Molecule Magnet with an Energy Barrier Exceeding 2000 K, *Chem. – Eur. J.*, 2021, **27**, 2623–2627.

7 K.-X. Yu, J. G. Kragskow, Y.-S. Ding, Y.-Q. Zhai, D. Reta, N. F. Chilton and Y.-Z. Zheng, Enhancing magnetic hysteresis in single-molecule magnets by ligand functionalization, *Chem*, 2020, **6**, 1777–1793.

8 A. B. Canaj, S. Dey, C. Wilson, O. Céspedes, G. Rajaraman and M. Murrie, Engineering macrocyclic high performance pentagonal bipyramidal Dy(III) single-ion magnets, *Chem. Commun.*, 2020, **56**, 12037–12040.

9 A. B. Canaj, M. K. Singh, C. Wilson, G. Rajaraman and M. Murrie, Chemical and in silico tuning of the magnetisation reversal barrier in pentagonal bipyramidal Dy(III) single-ion magnets, *Chem. Commun.*, 2018, **54**, 8273–8276.

10 Y. C. Chen, J. L. Liu, Y. Lan, Z. Q. Zhong, A. Mansikkamäki, L. Ungur, Q. W. Li, J. H. Jia, L. F. Chibotaru and J. B. Han, Dynamic Magnetic and Optical Insight into a High Performance Pentagonal Bipyramidal Dy(III) Single–Ion Magnet, *Chem. – Eur. J.*, 2017, **23**, 5708–5715.

11 A. Sarkar and G. Rajaraman, Modulating magnetic anisotropy in Ln(III) single-ion magnets using an external electric field, *Chem. Sci.*, 2020, **11**, 10324–10330.

12 K. R. Meihaus, M. E. Fieser, J. F. Corbey, W. J. Evans and J. R. Long, Record High Single-Ion Magnetic Moments Through $4f^n5d^1$ Electron Configurations in the Divalent Lanthanide Complexes $[(C_5H_4SiMe_3)_3Ln]^-$, *J. Am. Chem. Soc.*, 2015, **137**, 9855–9860.

13 M. R. MacDonald, J. E. Bates, J. W. Ziller, F. Furche and W. J. Evans, Completing the series of +2 ions for the lanthanide elements: synthesis of molecular complexes of Pr^{2+}, Gd2+, Tb2+, and Lu2+, *J. Am. Chem. Soc.*, 2013, **135**, 9857–9868.

14 C. A. Gould, K. R. McClain, J. M. Yu, T. J. Groshens, F. Furche, B. G. Harvey and J. R. Long, Synthesis and magnetism of neutral, linear metallocene complexes of terbium (II) and dysprosium(II), *J. Am. Chem. Soc.*, 2019, **141**, 12967–12973.

15 T. Simler, K. N. McCabe, L. Maron and G. Nocton, CO reductive oligomerization by a divalent thulium complex and CO_2^- induced functionalization, *Chem. Sci.*, 2022, **13**, 7449–7461.

16 W. Zhang, A. Muhtadi, N. Iwahara, L. Ungur and L. F. Chibotaru, Magnetic anisotropy in divalent lanthanide compounds, *Angew. Chem., Int. Ed.*, 2020, **59**, 12720–12724.

17 M. K. Assefa, G. Wu and T. W. Hayton, Synthesis of a terminal Ce(IV) oxo complex by photolysis of a Ce(III) nitrate complex, *Chem. Sci.*, 2017, **8**, 7873–7878.

18 L. A. Solola, A. V. Zabula, W. L. Dorfner, B. C. Manor, P. J. Carroll and E. J. Schelter, Cerium(IV) imido complexes: structural, computational, and reactivity studies, *J. Am. Chem. Soc.*, 2017, **139**, 2435–2442.

19 T. P. Gompa, A. Ramanathan, N. T. Rice and H. S. La Pierre, The chemical and physical properties of tetravalent lanthanides: Pr, Nd, Tb, and Dy, *Dalton Trans.*, 2020, **49**, 15945–15987.

20 C. T. Palumbo, I. Zivkovic, R. Scopelliti and M. Mazzanti, Molecular complex of Tb in the +4 oxidation state, *J. Am. Chem. Soc.*, 2019, **141**, 9827–9831.

21 A. R. Willauer, I. Douair, A.-S. Chauvin, F. Fadaei-Tirani, J.-C. G. Bünzli, L. Maron and M. Mazzanti, Structure, reactivity and luminescence studies of triphenylsiloxide complexes of tetravalent lanthanides, *Chem. Sci.*, 2022, **13**, 681–691.

22 Q. Zhang, S. X. Hu, H. Qu, J. Su, G. Wang, J. B. Lu, M. Chen, M. Zhou and J. Li, Pentavalent lanthanide compounds: formation and characterization of praseodymium (V) oxides, *Angew. Chem., Int. Ed.*, 2016, **55**, 6896–6900.

23 B. Monteiro, N. A. Bandeira, C. Lourenço, A. F. Lucena, J. M. Carretas, J. K. Gibson and J. Marçalo, Chemical evidence of the stability of praseodymium(V) in gas-phase oxide nitrate complexes, *Chem. Commun.*, 2019, **55**, 14139–14142.

24 S.-X. Hu, J. Jian, J. Su, X. Wu, J. Li and M. Zhou, Pentavalent lanthanide nitride-oxides: NPrO and $NPrO^-$ complexes with N [triple bond, length as m-dash] Pr triple bonds, *Chem. Sci.*, 2017, **8**, 4035–4043.

25 M. Briganti, F. Santanni, L. Tesi, F. Totti, R. Sessoli and A. Lunghi, A complete ab initio view of Orbach and Raman spin–lattice relaxation in a dysprosium coordination compound, *J. Am. Chem. Soc.*, 2021, **143**, 13633–13645.

26 J. G. Kragskow, A. Mattioni, J. K. Staab, D. Reta, J. M. Skelton and N. F. Chilton, Spin–phonon coupling and magnetic relaxation in single-molecule magnets, *Chem. Soc. Rev.*, 2023, **52**, 4567–4585.

27 L. Ungur and L. F. Chibotaru, Magnetic anisotropy in the excited states of low symmetry lanthanide complexes, *Phys. Chem. Chem. Phys.*, 2011, **13**, 20086–20090.

28 S. K. Singh, T. Gupta and G. Rajaraman, Magnetic anisotropy and mechanism of magnetic relaxation in Er(III) single-ion magnets, *Inorg. Chem.*, 2014, **53**, 10835–10845.

29 A. C. Parambil and A. Mansikkamäki, Nature of the Metal–Ligand Bonding in Bis (Cyclopentadienyl) and Bis (Cyclobutadienyl) Lutetium(III) Metallocenes, *J. Organomet. Chem.*, 2024, **1007**, 123024.

30 T. Vitova, P. Roesky and S. Dehnen, Open questions on bonding involving lanthanide atoms, *Commun. Chem.*, 2022, **5**, 12.

31 M. Briganti, G. F. Garcia, J. Jung, R. Sessoli, B. Le Guennic and F. Totti, Covalency and magnetic anisotropy in lanthanide single molecule magnets: the DyDOTA archetype, *Chem. Sci.*, 2019, **10**, 7233–7245.

32 S. Sugano, *Multiplets of transition-metal ions in crystals*, Elsevier, 2012.

33 O. G. Holmes and D. S. McClure, Optical spectra of hydrated ions of the transition metals, *J. Chem. Phys.*, 1957, **26**, 1686–1694.

34 L. Ungur, M. Thewissen, J.-P. Costes, W. Wernsdorfer and L. F. Chibotaru, Interplay of strongly anisotropic metal ions in magnetic blocking of complexes, *Inorg. Chem.*, 2013, **52**, 6328–6337.

35 W. Cai, C.-H. Chen, N. Chen and L. Echegoyen, Fullerenes as nanocontainers that stabilize unique actinide species inside: structures, formation, and reactivity, *Acc. Chem. Res.*, 2019, **52**, 1824–1833.

36 A. Svitova, K. Ghiassi, C. Schlesier, K. Junghans, Y. Zhang, M. Olmstead, A. Balch, L. Dunsch and A. Popov, Endohedral fullerene with μ3-carbido ligand and titanium-carbon double bond stabilized inside a carbon cage, *Nat. Commun.*, 2014, **5**, 3568.

37 K. Katoh, J. Sato, R. Nakanishi, F. Ara, T. Komeda, Y. Kuwahara, T. Saito, B. K. Breedlove and M. Yamashita, Terbium(III) bis-phthalocyaninato single-molecule magnet encapsulated in a single-walled carbon nanotube, *J. Mater. Chem. C*, 2021, **9**, 10697–10704.

38 M. C. G. López, F. Moro, A. La Torre, C. J. Gómez-García, P. D. Brown, J. Van Slageren and A. N. Khlobystov, Encapsulation of single-molecule magnets in carbon nanotubes, *Nat. Commun.*, 2011, **2**, 407.

39 G. Velkos, W. Yang, Y.-R. Yao, S. M. Sudarkova, F. Liu, S. M. Avdoshenko, N. Chen and A. A. Popov, Metallofullerene single-molecule magnet $Dy_2O@C_{2v}$ (5)-C_{80} with a strong antiferromagnetic Dy|Dy coupling, *Chem. Commun.*, 2022, **58**, 7164–7167.

40 S. Ito, R. Nakanishi, K. Katoh, B. K. Breedlove, T. Sato, Z.-Y. Li, Y. Horii, M. Wakizaka and M. Yamashita, Comparison between $DySc_2N@C_{80}$ and Dy_2 $ScN@C_{80}$ single-molecule magnetic metallofullerenes encapsulated in single-wall carbon nanotubes, *Dalton Trans.*, 2022, **51**, 6339–6344.

41 R. Nakanishi, J. Satoh, K. Katoh, H. Zhang, B. K. Breedlove, M. Nishijima, Y. Nakanishi, H. Omachi, H. Shinohara and M. Yamashita, $DySc_2N@C_{80}$ single-molecule magnetic metallofullerene encapsulated in a single-walled carbon nanotube, *J. Am. Chem. Soc.*, 2018, **140**, 10955–10959.

42 W. m. Rasmus, D. Jan, P. Cinthia, M. Matthias, W. Stephen, B. Harald, R. Stefano, N. Frithjof, P. Alexey, Y. Shangfeng, L. Dunsch and T. Greber, An Endohedral Single-Molecule Magnet with Long Relaxation Times: $DySc_2N@C_{80}$, *J. Am. Chem. Soc.*, 2012, **134**, 9840–9843.

43 M. K. Singh, N. Yadav and G. Rajaraman, Record high magnetic exchange and magnetization blockade in $Ln_2@C_{79}N$ (Ln = Gd(III) and Dy(III)) molecules: a theoretical perspective, *Chem. Commun.*, 2015, **51**, 17732–17735.

44 R. Nabi, R. K. Tiwari and G. Rajaraman, In silico strategy to boost stability, axiality, and barrier heights in dysprocenium SIMs via SWCNT encapsulation, *Chem. Commun.*, 2021, **57**, 11350–11353.

45 T. Sharma, M. K. Singh, R. Gupta, M. Khatua and G. Rajaraman, In silico design to enhance the barrier

height for magnetization reversal in Dy(III) sandwich complexes by stitching them under the umbrella of corannulene, *Chem. Sci.*, 2021, **12**, 11506–11514.

46 Y. Wang, J. Xiong, J. Su, Z. Hu, F. Ma, R. Sun, X. Tan, H.-L. Sun, B.-W. Wang and Z. Shi, $Dy_2@C_{79}N$: a new member of dimetalloazafullerenes with strong single molecular magnetism, *Nanoscale*, 2020, **12**, 11130–11135.

47 F. Liu, D. S. Krylov, L. Spree, S. M. Avdoshenko, N. A. Samoylova, M. Rosenkranz, A. Kostanyan, T. Greber, A. U. Wolter and B. Büchner, Single molecule magnet with an unpaired electron trapped between two lanthanide ions inside a fullerene, *Nat. Commun.*, 2017, **8**, 16098.

48 H. Zhang, R. Nakanishi, T. Yoshida, M. Nishijima, K. Harano, Y. Horii and M. Yamashita, First Encapsulation of Organometallic Single–Molecule Magnet into Single–Walled Carbon Nanotubes, *Angew. Chem. Int. Ed.*, 2025, e202503979.

49 P. B. Jin, K. X. Yu, Q. C. Luo, Y. Y. Liu, Y. Q. Zhai and Y. Z. Zheng, Tetraanionic arachno–Carboranyl Ligand Imparts Strong Axiality to Terbium(III) Single–Molecule Magnets, *Angew. Chem. Int. Ed.*, 2022, **61**, e202203285.

50 P. B. Jin, Y. Q. Zhai, K. X. Yu, R. E. Winpenny and Y. Z. Zheng, Dysprosiacarboranes as Organometallic Single–Molecule Magnets, *Angew. Chem., Int. Ed.*, 2020, **59**, 9350–9354.

51 A. R. Willauer, C. T. Palumbo, F. Fadaei-Tirani, I. Zivkovic, I. Douair, L. Maron and M. Mazzanti, Accessing the+ IV oxidation state in molecular complexes of praseodymium, *J. Am. Chem. Soc.*, 2020, **142**, 5538–5542.

52 B. Yin and C.-C. Li, A method to predict both the relaxation time of quantum tunneling of magnetization and the effective barrier of magnetic reversal for a Kramers single-ion magnet, *Phys. Chem. Chem. Phys.*, 2020, **22**, 9923–9933.

53 B. Yin and L. Luo, The anisotropy of the internal magnetic field on the central ion is capable of imposing great impact on the quantum tunneling of magnetization of Kramers single-ion magnets, *Phys. Chem. Chem. Phys.*, 2021, **23**, 3093–3105.

54 D. Aravena, Ab initio prediction of tunneling relaxation times and effective demagnetization barriers in kramers lanthanide single-molecule magnets, *J. Phys. Chem. Lett.*, 2018, **9**, 5327–5333.

55 A. Castro-Alvarez, Y. Gil, L. Llanos and D. Aravena, High performance single-molecule magnets, Orbach or Raman relaxation suppression?, *Inorg. Chem. Front.*, 2020, **7**, 2478–2486.

56 F. Lu, W.-X. Guo and Y.-Q. Zhang, Largely enhancing the blocking energy barrier and temperature of a linear cobalt (II) complex through the structural distortion: a theoretical exploration, *Inorg. Chem.*, 2021, **61**, 295–301.

57 X. Wu, J.-F. Li and B. Yin, The interpretation and prediction of lanthanide single-ion magnets from ab initio electronic structure calculation: the capability and limit, *Dalton Trans.*, 2022, **51**, 14793–14816.

58 Q.-Q. Yang, Y.-F. Wang, Y.-X. Wang, M.-J. Tang and B. Yin, Ab initio prediction of key parameters and magneto-structural correlation of tetracoordinated lanthanide single-ion magnets, *Phys. Chem. Chem. Phys.*, 2023, **25**, 18387–18399.

59 Y.-F. Wang, Y.-X. Wang, Q.-Q. Yang and B. Yin, Auxiliary Rather Than Dominant. The Role of Direct Dy–S Coordination in Single-Molecule Magnet Unveiled via ab initio Study, *J. Phys. Chem. A*, 2024, **128**, 5285–5297.

60 P. J. Stephens, F. J. Devlin, C. F. Chabalowski and M. J. Frisch, Ab initio calculation of vibrational absorption and circular dichroism spectra using density functional force fields, *J. Phys. Chem.*, 1994, **98**, 11623–11627.

61 C. Lee, W. Yang and R. G. Parr, Development of the Colle-Salvetti correlation-energy formula into a functional of the electron density, *Phys. Rev. B:Condens. Matter Mater. Phys.*, 1988, **37**, 785.

62 A. D. Becke, Density-functional exchange-energy approximation with correct asymptotic behavior, *Phys. Rev. A*, 1988, **38**, 3098.

63 M. Frisch, G. Trucks, H. B. Schlegel, G. E. Scuseria, M. A. Robb, J. R. Cheeseman, G. Scalmani, V. Barone, B. Mennucci and G. Petersson, *Gaussian 09, Revision d. 01*, Gaussian, Inc., Wallingford CT, 2009, vol. **201**.

64 D. Andrae, U. Haeussermann, M. Dolg, H. Stoll and H. Preuss, Energy-adjusted ab initio pseudopotentials for the second and third row transition elements, *Theor. Chim. Acta*, 1990, **77**, 123–141.

65 P. C. Hariharan and J. A. Pople, The influence of polarization functions on molecular orbital hydrogenation energies, *Theor. Chim. Acta*, 1973, **28**, 213–222.

66 F. Ortu, D. Reta, Y.-S. Ding, C. A. Goodwin, M. P. Gregson, E. J. McInnes, R. E. Winpenny, Y.-Z. Zheng, S. T. Liddle and D. P. Mills, Studies of hysteresis and quantum tunnelling of the magnetisation in dysprosium(III) single molecule magnets, *Dalton Trans.*, 2019, **48**, 8541–8545.

67 J. G. Kragskow, J. Marbey, C. D. Buch, J. Nehrkorn, M. Ozerov, S. Piligkos, S. Hill and N. F. Chilton, Analysis of vibronic coupling in a 4f molecular magnet with FIRMS, *Nat. Commun.*, 2022, **13**, 825.

68 G. Rajaraman, F. Totti, A. Bencini, A. Caneschi, R. Sessoli and D. Gatteschi, Density functional studies on the exchange interaction of a dinuclear Gd(III)–Cu(II) complex: method assessment, magnetic coupling mechanism and magneto-structural correlations, *Dalton Trans.*, 2009, 3153–3161.

69 R. F. Bader, Atoms in molecules, *Acc. Chem. Res.*, 1985, **18**, 9–15.

70 Y.-M. Chen, C.-Z. Wang, Q.-Y. Wu, J.-H. Lan, Z.-F. Chai, C.-M. Nie and W.-Q. Shi, Complexation of trivalent lanthanides and actinides with diethylenetriaminepentaacetic acid: Theoretical unraveling of bond covalency, *J. Mol. Liq.*, 2020, **299**, 112174.

71 T. Gupta, G. Velmurugan, T. Rajeshkumar and G. Rajaraman, Role of Lanthanide-Ligand bonding in the magnetization relaxation of mononuclear single-ion magnets: a case study on Pyrazole and Carbene ligated LnIII (Ln = Tb, Dy, Ho, Er) complexes, *J. Chem. Sci.*, 2016, **128**, 1615–1630.

72 K. Jeong, H. J. Jeong, S. M. Woo and S. Bae, Prediction of binding stability of Pu(IV) and PuO2(VI) by nitrogen tridentate ligands in aqueous solution, *Int. J. Mol. Sci.*, 2020, **21**, 2791.

73 F. Neese, F. Wennmohs, U. Becker and C. Riplinger, The ORCA quantum chemistry program package, *J. Chem. Phys.*, 2020, **152**, 224108.

74 F. Aquilante, J. Autschbach, R. K. Carlson, L. F. Chibotaru, M. G. Delcey, L. De Vico, I. F. Galván, N. Ferré, L. M. Frutos and L. Gagliardi, Molcas 8: New capabilities for multiconfigurational quantum chemical calculations across the periodic table, *J. Comp. Chem.*, 2016, **37**(5), 506–541.

75 L. F. Chibotaru and L. Ungur, Ab initio calculation of anisotropic magnetic properties of complexes. I. Unique definition of pseudospin Hamiltonians and their derivation, *J. Chem. Phys.*, 2012, **137**, 064112.

76 A. A. Granovsky, Extended multi-configuration quasi-degenerate perturbation theory: The new approach to multi-state multi-reference perturbation theory, *J. Chem. Phys.*, 2011, **134**, 214113.

77 B. r. O. Roos, R. Lindh, P.-Å. Malmqvist, V. Veryazov, P.-O. Widmark and A. C. Borin, New relativistic atomic natural orbital basis sets for lanthanide atoms with applications to the Ce diatom and LuF3, *J. Phys. Chem. A*, 2008, **112**, 11431–11435.

78 L. Ungur and L. F. Chibotaru, Ab initio crystal field for lanthanides, *Chem. – Eur. J.*, 2017, **23**, 3708–3718.

79 P. Å. Malmqvist, B. O. Roos and B. Schimmelpfennig, The restricted active space (RAS) state interaction approach with spin–orbit coupling, *Chem. Phys. Lett.*, 2002, **357**, 230–240.

80 K. Andersson, P. Å. Malmqvist, B. O. Roos, A. J. Sadlej and K. Wolinsk, Second–order perturbation theory with a complete active space self–consistent field reference function, *J. Phys. Chem.*, 1990, **94**, 5483–5488.

81 J. Jung, M. Atanasov and F. Neese, Ab initio ligand-field theory analysis and covalency trends in actinide and lanthanide free ions and octahedral complexes, *Inorg. Chem.*, 2017, **56**, 8802–8816.

82 S. Dey, T. Sharma and G. Rajaraman, Unravelling the role of spin–vibrational coupling in designing high-performance pentagonal bipyramidal Dy(III) single ion magnets, *Chem. Sci.*, 2024, **15**, 6465–6477.

83 A. L. Blockmon, A. Ullah, K. D. Hughey, Y. Duan, K. R. O'Neal, M. Ozerov, J. J. Baldoví, J. Aragó, A. Gaita-Ariño and E. Coronado, Spectroscopic analysis of vibronic relaxation pathways in molecular spin qubit [Ho (W5O18) 2] 9−: sparse spectra are key, *Inorg. Chem.*, 2021, **60**, 14096–14104.

84 **https://cccbdb.nist.gov/vsfx.asp.**